

Analysis of the formation of solar spectral lines with LTE

part 1

Elisabeth Strøm

November 27, 2017

1 Introduction

Here are the results from the first part of the SSB project, where we look at the FALC model of the solar atmosphere. In order to perform a stratification of the solar atmosphere, we will use the data from the FALC model (Fontela et al., 1993). In this model we assume that the solar atmosphere is in hydrostatic equilibrium and that it can be divided into horizontally homogeneous plane parallel layers. We will also make a comparison between the parameters of the Sun and that of the Earth's atmosphere (Allen, 1976).

2 Results

The FALC data consists of values for the height h where $h = 0$ km and the corresponding radial optical depth τ_{500} . The height $h = 0$ km is defined to be where $\tau_{500} = 1$. The other corresponding variables are the column mass m in units of g cm^{-2} , which is the mass a column of cross-section 1 cm^2 have above a height h . The temperature T is in units of K, n_{H} , n_{p} , n_{e} are the number densities of Hydrogen, free protons and free electrons, respectively, in units of cm^{-3} , and ρ is the gas density in units of g cm^{-3} . The total pressure P_{tot} is in units of dyn cm^{-2} , and is the sum of the gas pressure P_{gas} and the turbulent pressure $P_t = \rho v_t^2/2$ given by the microturbulent velocity v_t which accounts for the Doppler broadening. We also get the gas pressure rate, $P_{\text{gas}}/P_{\text{tot}}$. The first thing we do is extract these quantities from a file into our computer program.

2.1 The Sun

The temperature T of the Sun at different height h is shown in Figure 1.

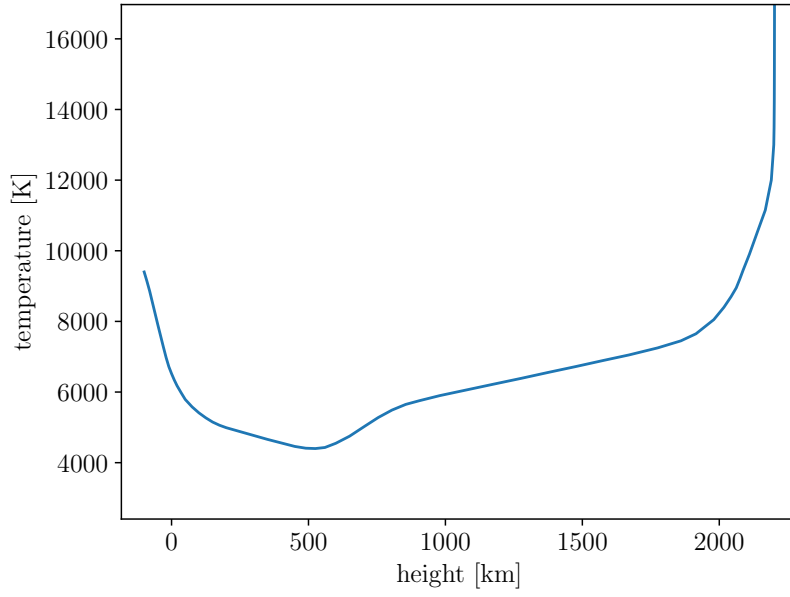


Figure 1: The temperature stratification. We see that this is the same as in the exercise text.

Assuming hydrostatic equilibrium, we can write the total pressure as

$$P_{\text{tot}} = gm, \quad (1)$$

where g is the gravity at a height h . We find the surface gravity g_{surface} by taking the average of P_{tot}/m , as the sun has no clearly defined surface. We find numerically that $g_{\text{surface}} = 27398.19 \text{ cm s}^{-2}$. The total pressure P_{tot} is shown against the column mass in Figure 2.

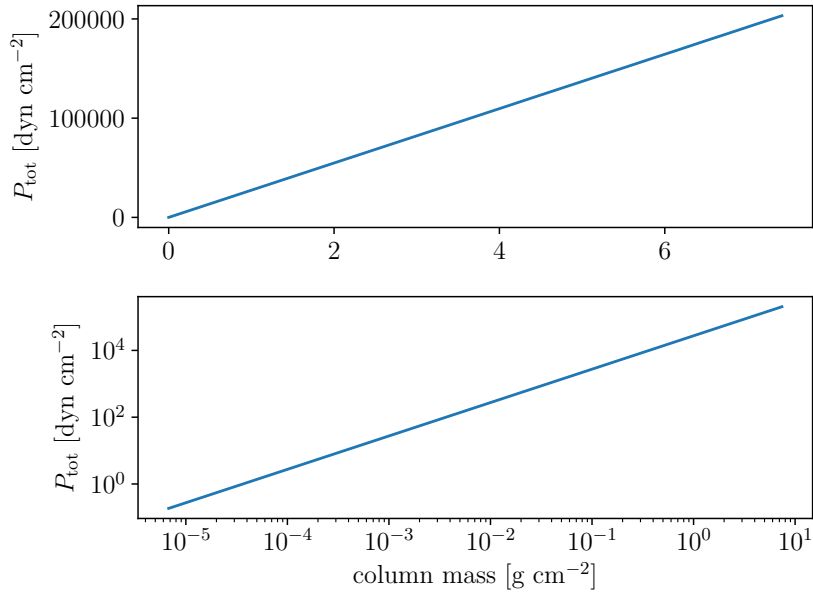


Figure 2: The total pressure plotted against the column mass. The top most subplot is in linear scales, while the lowest subplot is in log scale. We see that in both cases, the quantities scale linearly, due to the assumption of hydrostatic equilibrium.

We wish to know the mix of elements as a function of height. While we can find the hydrogen mass density by using the relation $\rho_H = n_H m_H$, to find the mass density of helium, we use that the abundance of helium compared to hydrogen is $n_{He} = 0.1 n_H$. We see that the mass ratio between the helium atom and the hydrogen atom is 3.97, $m_{He} = 3.97 m_H$.

The ratio of hydrogen and helium matter density to the total mass density ρ can be seen in Figure 3. We find that the fraction of the total mass density that is made up of metals, is $\rho_Z/\rho = 0.002226$

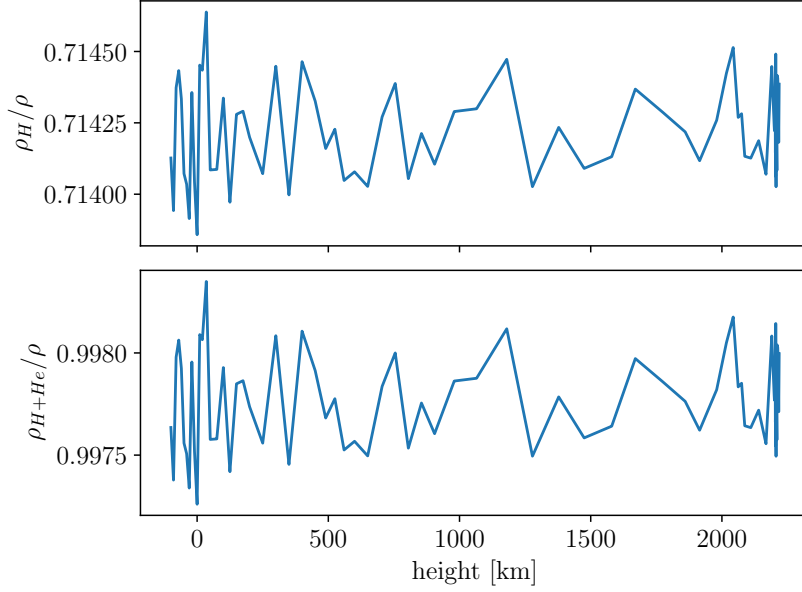


Figure 3: The first plot show the hydrogen mass density to total mass density ratio, the second is of the hydrogen plus the helium mass density fraction. For just hydrogen, the ratio varies between 0.7146 at the largest, and 0.7139 at the lowest, which is a difference of 0.07802%. For hydrogen and helium, the maximum and minimum value of the ratio is 0.9983 and 0.9973, respectively. This gives a difference of 0.1090 %. So the element mix is practically constant with height and the assumption of complete mixing is valid.

Column mass against height is shown in Figure 4.

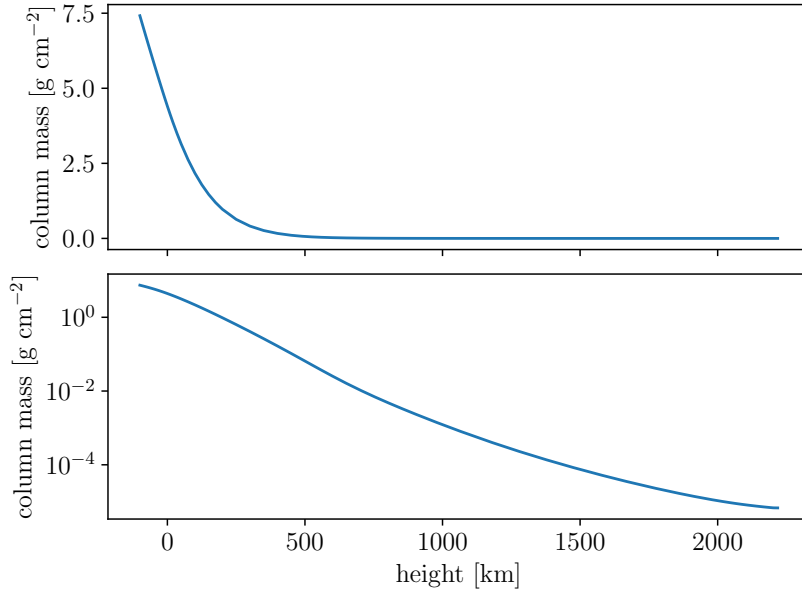


Figure 4: The column mass m is shown against height h . The left plot is in linear scales, while in the right, the y -axis is log-scaled. From the left plot it appears that the column mass is close to an exponential function of h , so we would expect a straight line when the y -axis is log scaled. We see in the left frame that this is exactly what we have, only the curve is not entirely linear, owing to the fact that m is not a complete exponential.

Gas density from the FALC model against height, and the analytical curve $\rho = \rho(h = -100 \text{ km})e^{-h/H_\rho}$ where $H_\rho \approx 147.31 \text{ km}$.

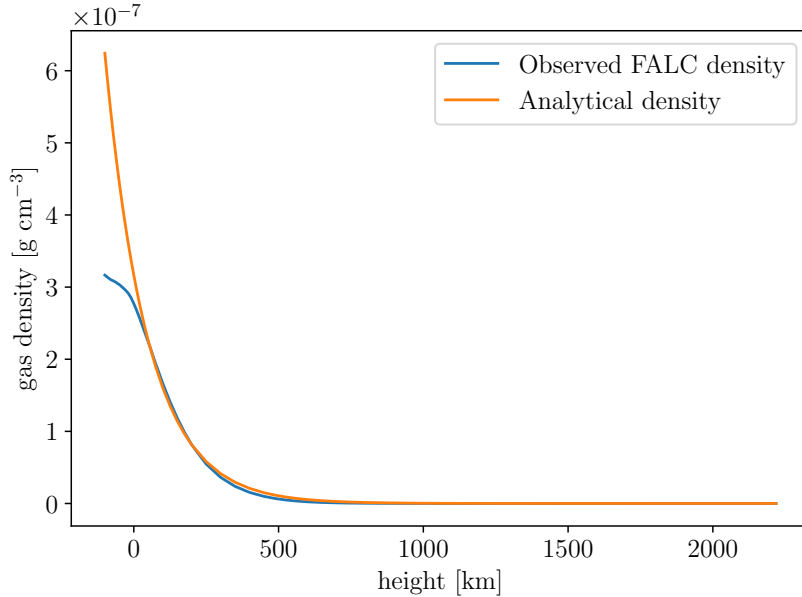


Figure 5: The blue curve shows the gas density against height computed from the FALC model data, while the orange curve comes from the expression $\rho = \rho(h = -100 \text{ km})e^{-h/H_\rho}$. $H_\rho \approx 147.31 \text{ km}$ was estimated using the least mean square method, comparing $\rho(H_\rho)$ with the observed density ρ , and using that $\rho(h = -100 \text{ km})$ is the density at the base of the photosphere.

The gas pressure against height is shown in Figure 6. By using the ideal gas law $P = nk_B T$, we can also plot the pressure caused just by the hydrogen and the free electrons, and that of helium.

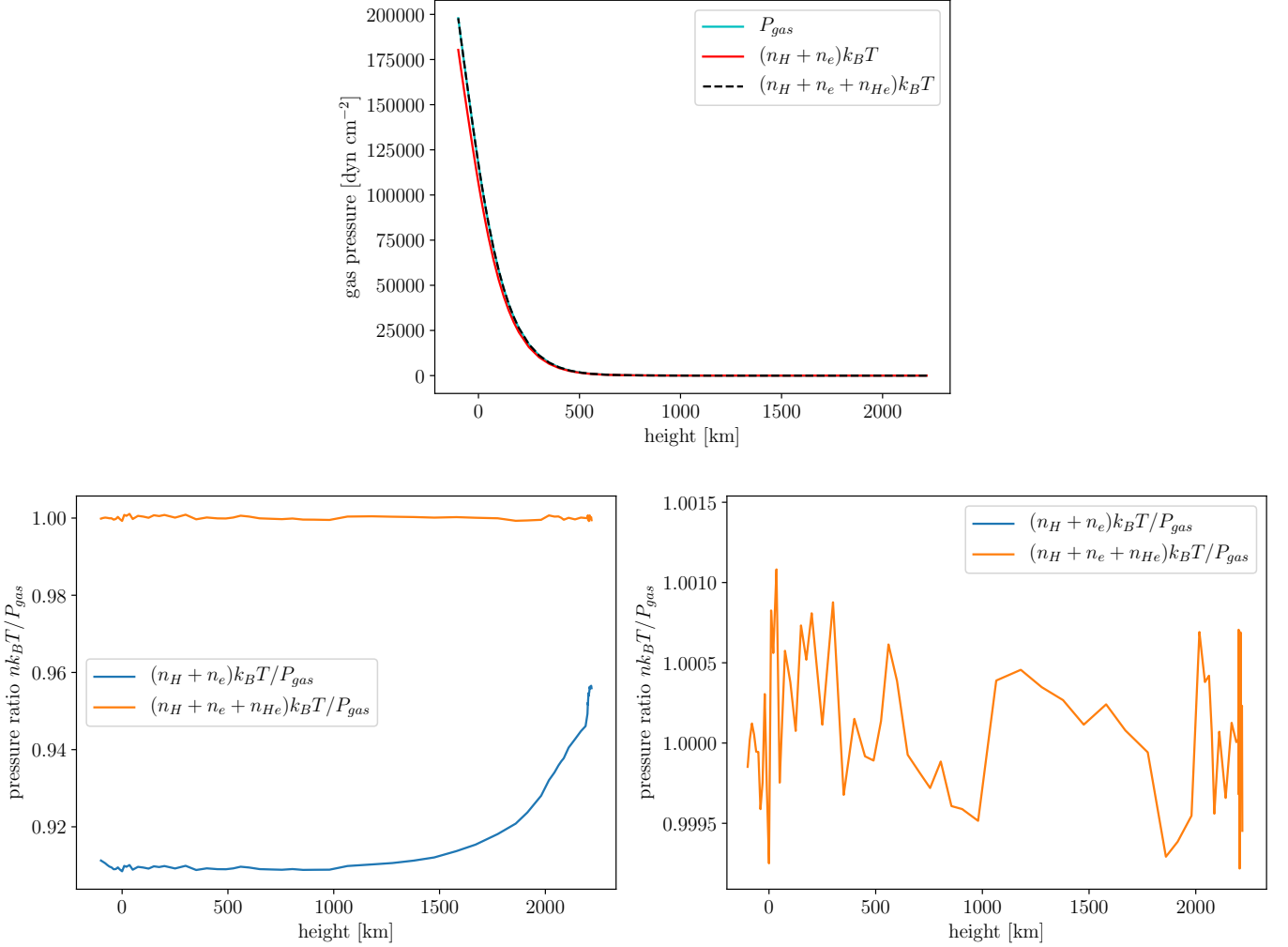


Figure 6: In the first plot, the blue line is of the gas pressure from the FALC model, the red line comes from calculating the hydrogen and electron pressure by using the ideal gas law, while the dashed black line comes from including the helium pressure. In the second plot, we see the ratio of the calculated pressure, and the observed pressure, in the two cases. We see that hydrogen and the free electrons alone is not responsible for the total gas pressure, although the $P_{\text{H+e}}/P_{\text{gas}}$ ratio (blue line, second frame) is over 0.9, and increases at bigger heights. This is also shown in the first frame, where the red and blue curve overlap better after $h \sim 900$ km, but visibly deviate from one another at smaller height. When we add the helium pressure, we see that the pressure ratio (orange line, second frame) is ca. 1, and that the curves in the first frame almost completely overlap. In the third frame is a close up of the $P_{\text{H+e+He}}/P_{\text{gas}}$ ratio, where we see that the deviations from 1, is less than of the order of 10^{-3} . The reason for this deviation, is that the gas of the Sun is not a complete ideal gas.

The number density of hydrogen, free electrons, free protons, and the free electrons that didn't come from ionized hydrogen, can be seen in Figure 7 against height, both in linear scales, and in log scales. We find the electrons that does not come from hydrogen by taking the total free electron density, and subtracting the proton density, $n_{\text{e, He+Z}} = n_{\text{e}} - n_{\text{p}}$.

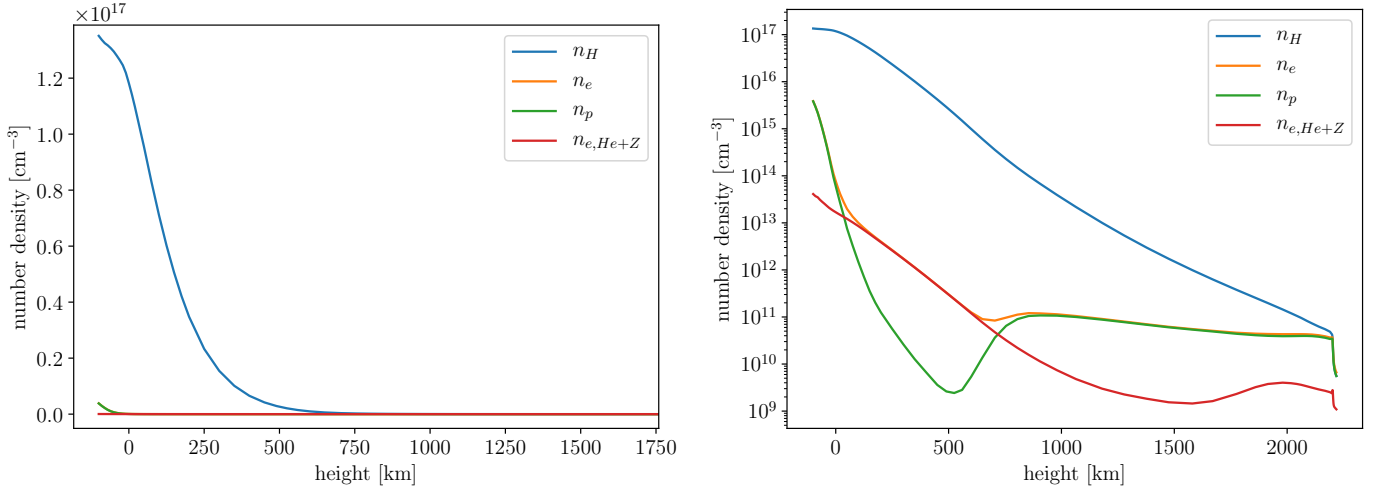


Figure 7: In the left frame is the number densities against height in linear scales, while in the right, the y-axis is in log scales. We see that $n_H \sim 10^{17} \text{ cm}^{-3}$ at most, and is almost 10 times larger than the proton and free electron density, and 10^3 times larger than non- H^+ free electrons. All the number densities decrease as we move outward from the center.

If we start from the outside and move inwards into the star, we see that from $h \sim 2200 \text{ km}$ to $h \sim 900 \text{ km}$, that the free electron contribution is dominated by ionized hydrogen, which we can observe as the n_p and n_e curves overlap almost perfectly in this region. Around $h \sim 2000 \text{ km}$, n_e is slightly larger than n_p , which correspond to a small “bump” in the $n_{e, He+Z}$ curve, meaning there is also a contribution from electrons from helium and the metals. In the range $h \sim 900 - 500 \text{ km}$, the proton density decreases, while the electron density goes slightly down before it increases (both the red and the orange line). This means that the free electron contribution comes mostly from the metals and helium at this point. This goes on from $h \sim 600 \text{ km}$ to $h \sim 250 \text{ km}$. We notice that the n_e curve is parallel to the n_H curve in this same range. This is because the number density of metals scale almost 1:1 with hydrogen, so when the electrons come mostly from ionized metals, the two curves will be parallel.

Past this, further into the Sun, the electrons come mostly from hydrogen again. The metals are very easy to ionize, but if we compare the proton number density curve with the temperature curve, we see that hydrogen is only ionized where the temperature is high; the minimum in the temperature in Figure 1, correspond to the dip in the n_p curve. We can see this better in the next figure

The ionized hydrogen to total hydrogen number density (ionized and neutral) fraction is shown in Figure 8.

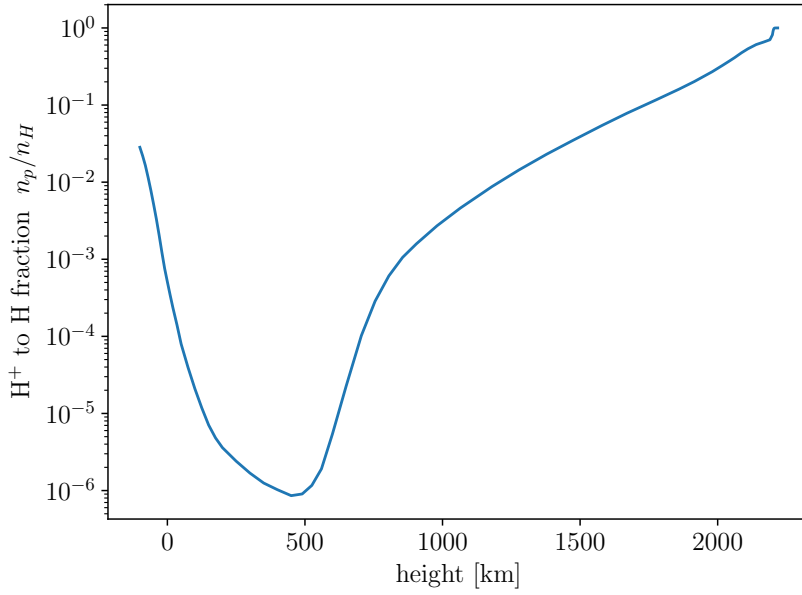


Figure 8: The number density of neutral and ionized hydrogen, can be described by the Saha-law, which contain an exponential of T , $e^{-\alpha/T}$, which is why when the temperature increases a small amount, the H^+ fraction increases even more, hence the n_p/n_H curve's tilt in comparison to Figure 1.

Deep in the photosphere, the photon density is approximately

$$n_{\text{photon}} \approx 20T^3, \quad (2)$$

while higher in the atmosphere, it is more accurately given by

$$n_{\text{photon}} \approx 20T_{\text{eff}}^3/2\pi, \quad (3)$$

where $T_{\text{eff}} = 5770$ K is the effective temperature of the Sun.

At the lowest model location, $h = -100$ km, the photon and hydrogen density is approximately $n_{\text{photon}} \approx 1.66 \cdot 10^3 \text{ cm}^{-3}$ and $n_H \approx 1.35 \cdot 10^{17} \text{ cm}^{-3}$, respectively, and their ratio is $n_{\text{photon}}/n_H \approx 0.0043$. So hydrogen is 10^3 times more abundant than photons at this height, which makes sense as this corresponds to an optical depth of $\tau_{500} = 23.65$, and we will see fewer photons escaping from here compared to higher up in the star.

At the highest location, $h = 2218.2$ km and $\tau_{500} = 0$, the densities are $n_{\text{photon}} \approx 6.12 \cdot 10^{11} \text{ cm}^{-3}$ and $n_H \approx 5.57 \cdot 10^9 \text{ cm}^{-3}$. The density ratio is 109.68, so now it is the photons that are more abundant, 100 times more abundant in fact. This is due to the gas here being more optically thin: The photons can easier escape the atmosphere without being absorbed by the gas particles, with the exception of those photons with the right energy to cause the $\text{Ly}\alpha$ line process to occur.

2.2 Earth

Now we look at our own planet, and plot various parameters for Earth's atmosphere. These parameters are taken from Allen (1976), and are the height h in km, the temperature T in K,

the gas density in g cm^{-3} , the total particle number density in cm^{-3} , and the pressure P in dyn cm^{-2} .

The temperature, the pressure, the gas density, and the number density are plotted against height, and can be seen in Figure 9.

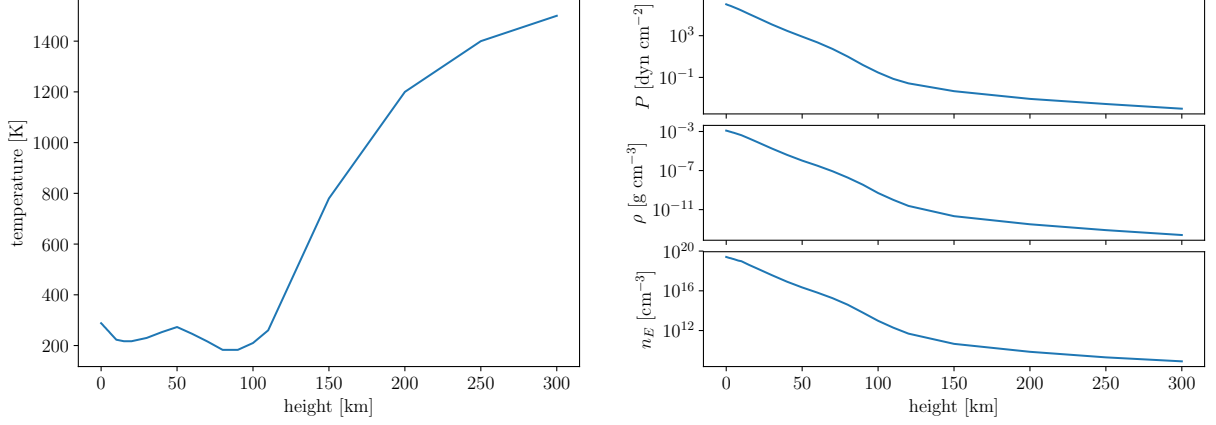


Figure 9: The temperature against height is seen to the left, while the pressure, gas density, and number density, can be seen to the right with a logarithmically scaled y -axis. We see that n_E , ρ and P all have almost the same shape. We see that the temperature increases considerably around $h \sim 100$ km. This is due to heating caused by absorption of UV radiation from the Sun in the thermosphere. The same occurs at $h \sim 20$ km due to the ozonelayer heating up through capture of UV photons.

The pressure and the gas density in normalized units are shown in Figure 10.

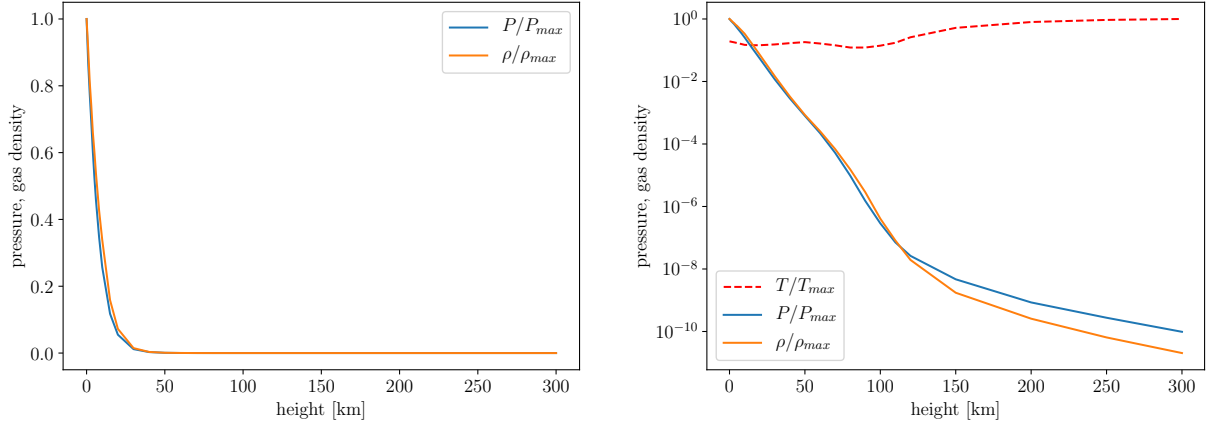


Figure 10: The normalized pressure and gas density against height is shown in linear scales to the left, and with a logarithmic y -axis to the right. The curves of the pressure and the gas density have the same shape, but the pressure will lie just below the gas density up to $h = 110$ km, after this it will lie above. This is because the pressure is a function of the temperature as well as the density, through the ideal gas law. If we over-plot the normalized temperature, the red dashed line, we see that the dips in this curve correspond to where the pressure curve goes below the density, while where the temperature increases, the pressure does as well.

In figure 11, the mean molecular weight is plotted against height.

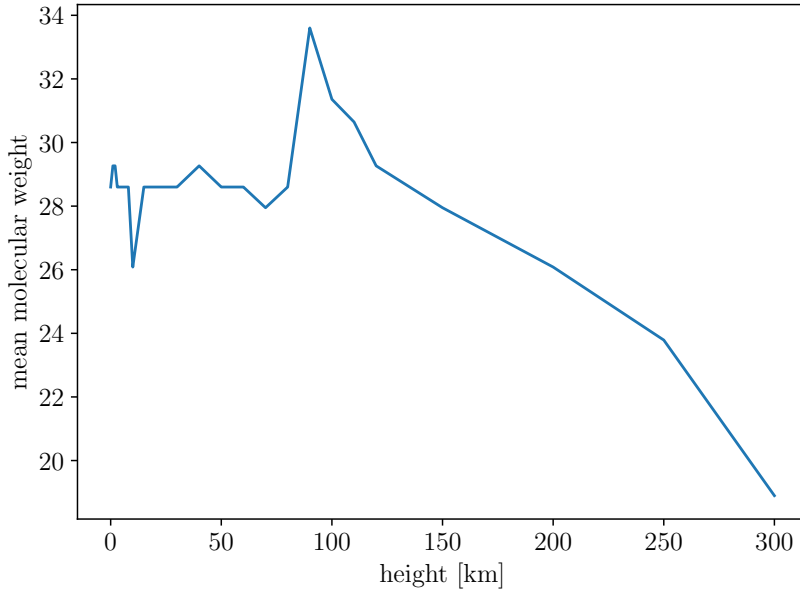


Figure 11: From around $h \sim 90$, the molecular weight start decreasing. In the high atmosphere, the air is very thin; from figures 9 and 10 we see the gas density is very small, and while the number density continues to decrease also, it is still larger than ρ . This means that the mean molecular weight will fall for high h .

The density scale height of the lower terrestrial atmosphere is found by using the formula

$$H_{\rho,E} = \frac{k_B T(0)}{\mu(0) m_H g_E} = 8.47 \text{ km}, \quad (4)$$

where g_E is the standard gravity at the Earth's surface, and $T(0)$ and $\mu(0)$ is the temperature and the mean molecular weight at $h = 0$ km. We see that this value is much smaller than that of the Sun, $H_{\rho,\odot} = 147.31$ km. This is because the temperature near the Earth's surface is around 300 K, much smaller than anywhere on the Sun. The mean molecular weight is also larger in the Earth's atmosphere, where the majority of the air consists of molecular nitrogen, whereas on the Sun, it is mostly hydrogen, electrons, and some helium. While the standard gravity g is larger on the Sun than on Earth, the much higher temperature of the Sun, still makes $H_{\rho,\odot}$ bigger than $H_{\rho,E}$.

If we compute the ratios between the parameter values of the Sun and the Earth at $h = 0$ km of each atmosphere, we find,

$$\frac{T_E}{T_\odot} = 0.044 \quad \frac{n_E(0)}{n_\odot(0)} = 197.48 \quad \frac{P_E(0)}{P_\odot(0)} = 8.48 \quad \frac{\rho_E(0)}{\rho_\odot(0)} = 4439.8 \quad \frac{m_E}{m_\odot} = 236.94. \quad (5)$$

So for every parameter, with the exception of the temperature, are the Earth's parameters larger than the Sun at this height. To find the column mass on Earth's surface, we used that $m(0) = P(0)_E / g_E = 1043.47 \text{ g cm}^{-2}$, where we have again assumed hydrostatic equilibrium. In comparison, the Sun's column mass at $h = 0$ km is only 4.40 g cm^{-2} . The reason for the large difference in parameter values, is, of course, that the Earth is a rock planet with a relatively thin atmosphere, while the Sun is a star where different processes occur, like fusion and convection, within the entirety of it, with no clearly defined surface. They are, essentially, two completely different objects.

In Figure 12, the gas particle number density in the Earth's atmosphere is plotted together with the photon number density at Earth and that produced at $h_{\odot} = 0$ in the Sun. The photons received at Earth has a number density given by

$$n_{\text{phot}} = \pi \frac{R^2}{D^2} n_{\text{phot}}^{\text{top}}, \quad (6)$$

where R is the solar radius, D is the distance from the Sun to the Earth, and $n_{\text{phot}}^{\text{top}}$ is defined in Equation 3, and where for $n_{\text{phot}}^{\odot}(0)$, we have used Equation 2.

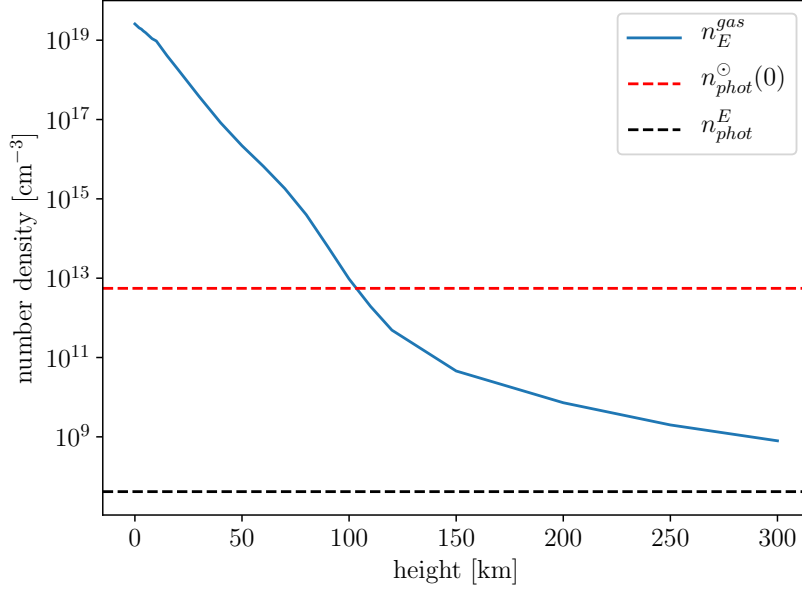


Figure 12: Number density of gas particles in Earth's atmosphere against height (blue), the photons received from the Sun (black), and the photons produced in the Sun at $h = 0$ (red). We see that around $h = 100$, $n_E = n_{\text{phot}}^{\odot}(0)$, and that the number density of photons in the Earth's atmosphere is smaller than the thermal production of photons in the Sun, and the gas particle number density at all heights.

References

C. W. Allen. *Astrophysical quantities*. London: University of London, Athlone Press, 1976.

J.M. Fontela, E.H. Avrett, and R. Loeser. *Astrophys. J*, 409:319, 1993.

Analysis of the solar continuum and solar extinction

Elisabeth Strøm¹
AST4310 25.09.2017

¹ Institute of Theoretical Astrophysics, University of Oslo

Abstract. We study the solar continuum at visible and near-infrared wavelengths.. Through comparison with Planck's law, and the FALC model (Fontela et al. 1993), we find that the computed intensity, where we only include H^- extinction, and astrophysical flux diverges from the observed one Allen (1976). This indicates that local thermodynamic equilibrium (LTE) may not be true throughout the entire star. This divergence can also be due to us not including the extinction by metals in our computed model. The LTE approximated curve from the FALC model provides the best fit, the maximum intensity and flux being lower than the observed ones, but the plotted curves as a function of wavelength otherwise showing an almost perfect fit. Comparing the mean height of formation ($\langle h \rangle$) with the height where the optical depth is equal to 1 ($h(\tau_\lambda = 1)$) and the height where the solar temperature is equal to the brightness temperature (T_b), we there are some discrepancies, but they are within acceptable bound. In addition, the ratio between the computed intensity and the Planck curve is on average 0.93, which we consider a good result. From this we conclude that the LTE Eddington-Barbier approximation is valid, and that H^- free-free and bound-free transitions are the major source of extinction in the Sun, along with Thomson scattering off free electrons.

1. Introduction

In this report we will show our attempt at reproducing the work of Chandrasekhar & Breen (1946). Like Chandrasekhar & Breen (1946), we will show that the solar continuum in the visible and infrared region is created as a result of H^- extinction. We will go over the conditions that allow this continuum to arise, drawing on the solar stratification we have presented in the first report.

We will also attempt to analyze the legibility of the Eddington-Barbier approximation, which states that the emergent intensity from the solar disk, is created at the place in the solar atmosphere where optical depth equals unity. We intend to do this by looking at the emergent intensity as a function of wavelength and frequency, the calculated mean formation height of this intensity along with where the optical depth equals unity for different wavelengths. From this we hope to see how assumptions of local thermodynamic equilibrium hold up in the photosphere and chromosphere of the Sun.

First we go through our methods and our sources of data, then we present our results before we discuss them in the next section. Finally follows our conclusions.

2. Method

Here we present the methods we have used to obtain the results in Section 3. All units are in cgs unless stated otherwise.

We will use data of intensity and astrophysical flux from Allen (1976) which contains the radially emergent intensity and the astrophysical flux in the solar continuum with smoothed lines, I_λ and F_λ , and without smoothed lines, I_λ^c and F_λ^c , all in units of $\text{erg cm}^{-2} \text{s}^{-1} \text{ster}^{-1} \mu\text{m}^{-1}$, as a function of wavelength in μm . The superscript c indicates quantities where the spectral lines are not smoothed. While flux emitted from a stellar disk is usually defined as $F_\lambda = \pi \text{ rad } I_\lambda$, astrophysical flux is usually written as $F_\lambda/(\pi \text{ rad})$, meaning it has the same units as the intensity.

Using the relation

$$\lambda I_\lambda = \nu I_\nu, \quad (1)$$

we can also convert these values from per wavelength $\Delta\lambda = 1 \mu\text{m}$ for the spectral bandwidth, to per frequency bandwidth $\Delta\nu = 1 \text{Hz}$. The units are now $\text{erg cm}^{-2} \text{s}^{-1} \text{ster}^{-1} \text{Hz}^{-1}$.

We wish to find the Planck curve that resembles the observed intensity the most. To do this we use Planck's law,

$$B_\lambda(T) = \frac{2hc^2}{\lambda^5} \frac{1}{e^{\frac{hc}{\lambda k_B T}} - 1}, \quad (2)$$

where T is the temperature, h is Planck's constant, λ is the wavelength, c the speed of light, and k_B is the Boltzmann constant. We then perform a least mean square analysis to determine at what temperature this most closely resembles the observed curve. Another way to do this is to find the brightness temperature directly.

The brightness temperature T_b is defined as the the temperature of the Planck curve that reproduces the observed intensity, $I = B(T_b)$. We find it by inverting Planck's function with respect to the temperature,

$$T_b = \frac{hc}{\lambda k_B} \frac{1}{\log\left(\frac{2hc^2}{I_\lambda \lambda^5} + 1\right)}. \quad (3)$$

We can now find the brightness temperature of the solar continuum as a function of wavelength.

We will assume that the total extinction α_λ is due primarily to bound-free and free-free interactions by H^- , which is accurate for wavelengths $\lambda > 0.5 \mu\text{m}$. This extinction, $\alpha_\lambda(H^-)$, has already been calculated by Gray (1992) in units of cm^2 per neutral hydrogen atom. Another source of extinction is Thomson scattering off free electrons. We use parameters from Fontela et al. (1993), which contains the optical thickness in the Sun as a function of height, along with the electron, proton and total hydrogen density at these heights, to compute the total extinction per cm, α_λ . The total extinction is

$$\alpha_\lambda = \alpha_\lambda(H^-) n_{\text{neutral H}} + \sigma^T n_e, \quad (4)$$

where $\sigma^T = 6.648 \cdot 10^{-25} \text{ cm}^2$ is the Thomson cross-section, $n_{\text{neutral H}}$ is the number density of neutral hydrogen, which we find by taking the total hydrogen number density minus the free proton number density. n_e is the free electron density.

As we know the stratification of the Sun (Fontela et al. 1993) and the continuous extinction, we can now calculate the corresponding optical depth. It is given by

$$\tau_\lambda(h_0) = - \int_\infty^{h_0} \alpha_\lambda dh, \quad (5)$$

at any height h_0 . We use the trapezoidal rule to solve this integral,

$$\tau_\lambda(h_0) = - \sum_{i=1}^N \frac{\alpha_\lambda(h_{i-1}) + \alpha_\lambda(h_i)}{2} \Delta h_i, \quad (6)$$

where $h_N = h_0$ and $\Delta h_i = h_{i+1} - h_i$. This too will be evaluated at $\lambda = 0.5 \mu\text{m}$.

The next we do is calculate the intensity of the emergent radiation from the center of the solar disk. Assuming plane-parallel stratification, the intensity is given by

$$I_\lambda = \int_0^\infty S_\lambda e^{-\tau_\lambda} d\tau_\lambda, \quad (7)$$

where S_λ is the source function. In this way we can compare the observed intensity with the computed one. From this we also have the intensity contribution function, which gives the emergent intensity contribution of each layer. It is defined as

$$\frac{dI_\lambda}{dh} = S_\lambda e^{-\tau_\lambda} \alpha_\lambda. \quad (8)$$

Its weighted mean defines the “mean height of formation”:

$$\langle h \rangle = \frac{\int_0^\infty h(dI_\lambda/dh)dh}{\int_0^\infty (dI_\lambda/dh)dh} = \frac{\int_0^\infty h S_\lambda e^{-\tau_\lambda} d\tau_\lambda}{\int_0^\infty S_\lambda e^{-\tau_\lambda} d\tau_\lambda}. \quad (9)$$

Here we have assumed local thermodynamic equilibrium (LTE), and we solve the integral in Equation 7 by use of the trapezoidal rule.

We can modify Equation 7 to account for intensity emerging from the Sun at an angle θ relative to our line of sight,

$$I_\lambda(0, \mu) = \int_0^\infty S_\lambda e^{-\tau_\lambda/\mu} d\tau_\lambda/\mu, \quad (10)$$

where $\mu = \cos \theta$, and the first argument in I_λ is height, meaning the intensity is evaluated at $h = 0 \text{ km}$, what we define as the surface of the Sun. We also define the radius of the apparent solar disk,

$$\frac{r}{R_\odot} = \sin \theta. \quad (11)$$

We can now integrate the emergent intensity over the emergence angle to get the emergent astrophysical flux,

$$F_\lambda(0) = 2 \int_0^1 I_\lambda(0, \mu) \mu d\mu, \quad (12)$$

evaluated at $h = 0 \text{ km}$. To do this we use an integration method that excludes the endpoint, seeing as this integral cannot be evaluated at $\mu = 0$. We will use a three-point-Gaussian integration defined as,

$$\int_{-1}^1 f(x) dx \approx \sum_{i=1}^n w_i f(x_i), \quad (13)$$

where the abscissa values x_i and weights w_i are found for orders $n = 2 - 10$ and higher in Abramowitz & Stegun (1964) on page 916. For our case, $f(x) = I(0, \mu)\mu$.

3. Results

The emergent continuum intensity and the astrophysical flux, with and without smoothed lines, in units of wavelength and frequency, can be seen in Figure 1, against wavelength. The maximum continuum intensity without smoothed lines is $I_\lambda^c = 4.6 \cdot 10^{10} \text{ erg cm}^{-2} \text{ s}^{-1} \text{ ster}^{-1} \mu\text{m}^{-1}$ at $\lambda = 0.41 \mu\text{m}$. In units of per frequency, this correspond to $I_\nu^c = 4.2055 \cdot 10^{-5} \text{ erg cm}^{-2} \text{ s}^{-1} \text{ ster}^{-1} \text{ Hz}^{-1}$.

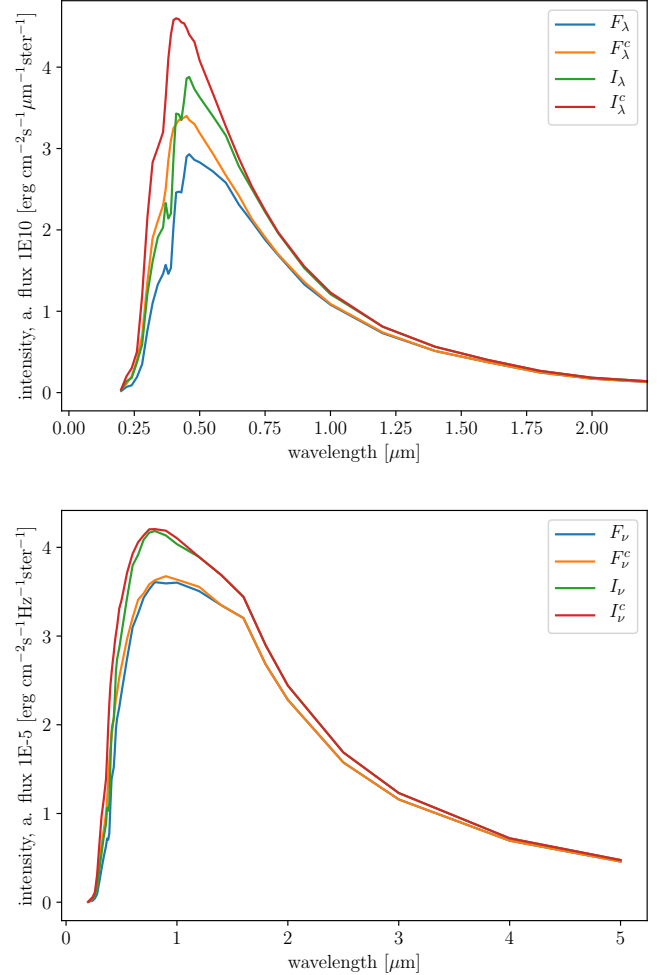


Fig. 1: Intensity and astrophysical flux in units of wavelength (top frame) and frequency (lower frame) against wavelength. Notice the different range of the x-axis. The intensity is larger than the astrophysical flux, and the non-smoothed parameters, larger than the smoothed ones.

The Planck function in units of per wavelength, fitted to the observed intensity can be seen in Figure 2. We see that it is not a total fit, the peak of the observed intensity having a larger value than the peak of the Planck curve, we will discuss why in the next section. The temperature of the Planck curve is $T \approx 6310 \text{ K}$.

In figure 3, we can see the brightness temperature of the observed solar continuum as a function of wavelength.

The total H^- extinction from Gray (1992) at the height $h = 0 \text{ km}$ in the FALC model (Fontela et al. 1993) can be seen in Figure 4 against wavelength.

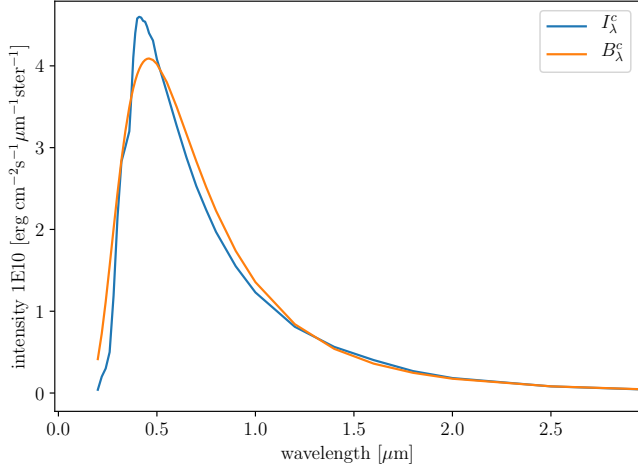


Fig. 2: The observed intensity without smoothed lines, I_λ^c per unit wavelength, and the best fitted Planck curve is shown above, both in units of $\text{erg cm}^{-2} \text{s}^{-1} \text{ster}^{-1} \mu\text{m}^{-1}$. We see that it is not a perfect fit, likely due to LTE not being valid everywhere in the Sun, and that we use a constant brightness temperature. The brightness temperature is here $T \approx 6310$ K.

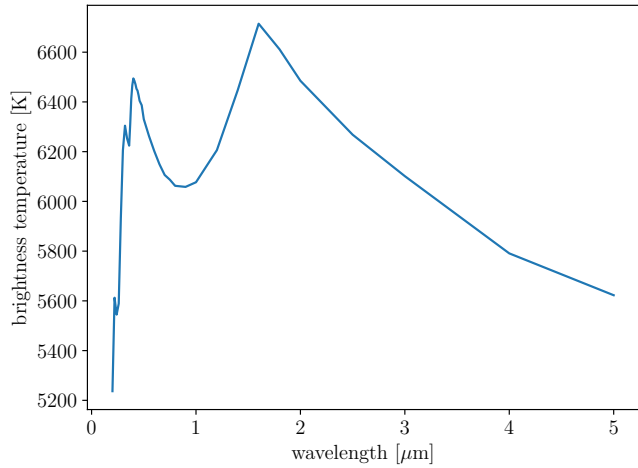


Fig. 3: Brightness temperature is on the vertical y -axis, the wavelength on the x -axis. The curve peaks at $\lambda = 1.6 \mu\text{m}$, with a lower peak at $\lambda = 0.4 \mu\text{m}$

The shape of the H^- extinction curve share similarities to the brightness temperature, which is better shown in Figure 5. We notice that as the dips in the temperature correspond to peaks in the extinction. This is due to a high temperature will easier ionize the H^- ions and neutral hydrogen, hindering the bound-free and free-free transitions, respectively. However, at the lowest wavelengths, the extinction decreases along with the brightness temperature. This is due to us not including extinction done by metals in our model ionization edges, which is found at the short wavelengths. This explains the “spikes” in the temperature curve before the peak at $\mu = 0.4 \mu\text{m}$. We will come back to this in the discussion section.

In Figure 6, we show the total extinction in the solar continuum. This consists mainly of the H^- extinction from Figure 4, but also of Thomson scattering off free electrons. They are shown separately, along with their sum. For low heights, the ex-

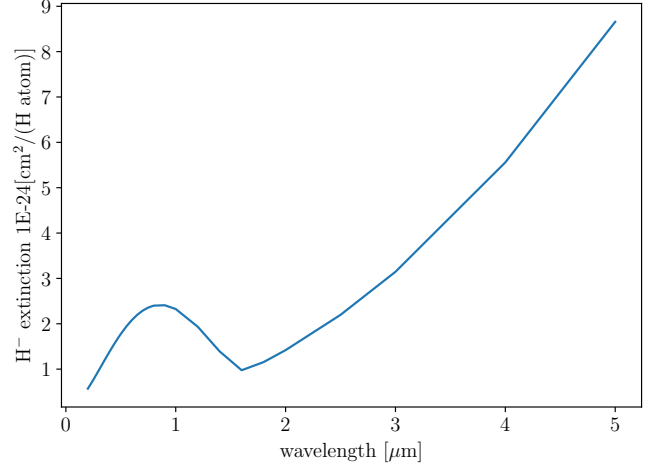


Fig. 4: Total H^- extinction at the surface of the FALC model (Fontela et al. 1993) of the sun, $h = 0$ km. On the x -axis is the wavelength

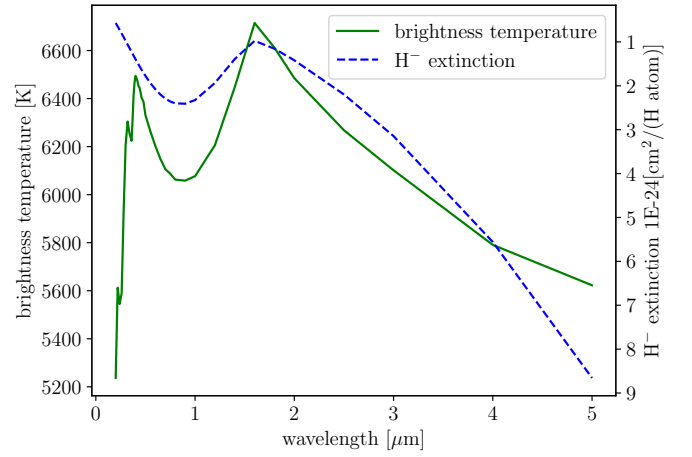


Fig. 5: The brightness temperature along with the inverted total H^- extinction against wavelength. The left vertical y -axis provides values for T_b , while the right vertical y -axis give the value of the extinction, which is inverted to better see the similarities between the two curves.

inction seem to be mainly due to H^- bound-free and free-free interactions. Higher up in the star, Thomson scattering seem to be the dominating factor. Both types of extinction increase as h decrease. This is due to the number density of hydrogen and free electrons increase deeper into the star. At around $h \sim 1000$ km, the two factors are equal.

The optical depth calculated by integrating the total extinction, along with the optical depth from the FALC model, can be seen in Figure 7. We see that around $h = 500$ km, the curves deviate slightly, but beyond that they follow almost the same curve. The reasons for this will be discussed in the next section.

The contribution functions for the wavelengths $\lambda = 0.5 \mu\text{m}$, $1 \mu\text{m}$, $1.6 \mu\text{m}$, and $5 \mu\text{m}$ can be seen in Figure 8.

In Table 1, we show the peak location of the contribution functions, the mean formation height, $\langle h \rangle$, the computed and the observed intensity and their ratio, and the black body intensity compared to the computed intensity. It also contains the brightness temperature and where $\tau_\lambda = 1$, the height where $T_b = T(h)$,

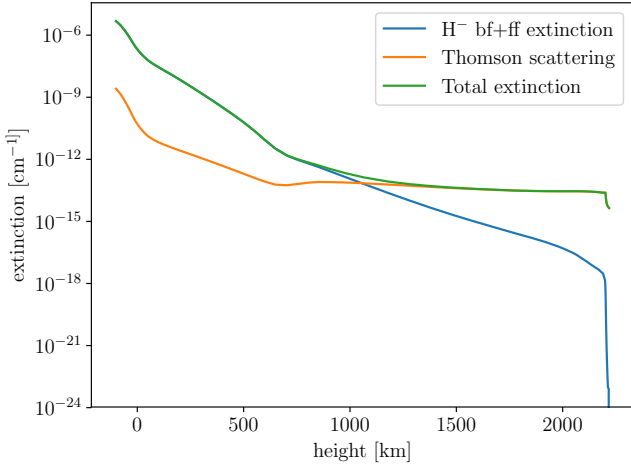


Fig. 6: Total extinction of the solar continuum at $\lambda = 0.5 \mu\text{m}$ is a sum of H^- extinction and Thomson scattering. The y -axis is log scaled, and on the x -axis is the height. For low heights, the extinction seem to be mainly due to H^- bound-free and free-free interactions. Higher up in the star, Thomson scattering seem to be the dominating factor. At around $h \sim 1000$ km, the two factors are equal.

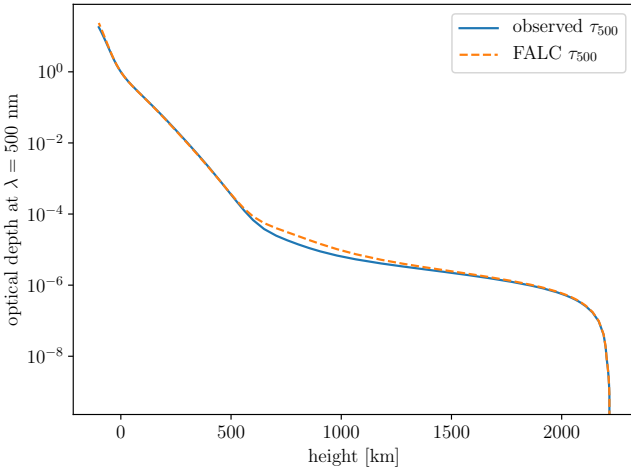


Fig. 7: The optical depth against height at $\lambda = 0.5 \mu\text{m}$. The y -axis is log scaled. Both the optical depth calculated from the total extinction, and the optical depth according to the FALC model is shown. We see that they are a close fit to each other. At around $h = 500$ km, there is a slight deviation, the integrated τ_{500} lying slightly below the FALC τ_{500} , but not by much.

along with this temperature $T(h)$, and the height where $\tau_\lambda = 1$ for the different wavelengths stated above and stated in the table.

Figure 9 shows the emergent intensity as a function of wavelength, against wavelength, both the intensity calculated by Allen (1976), and the computed intensity using the temperature data from the FALC model (Fontela et al. 1993) and the wavelength from Allen. We see that the curves are a good fit up to around $0.5 \mu\text{m}$ where both the curves peak, but the intensity from Allen (1976) has a smaller maximum value than that computed from the FALC model. Again, this can be due to the lack of metal extinction in our model. The same can be seen in Figure 12

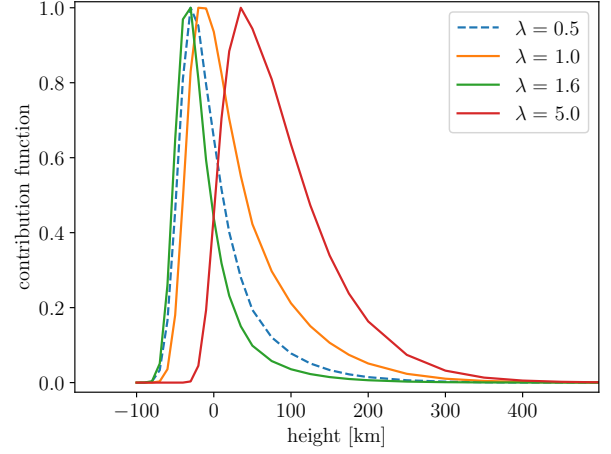


Fig. 8: The normalized contribution functions for the wavelengths $\lambda = 0.5, 1.0, 1.6$ and $5 \mu\text{m}$ is on the y -axis, while the height h is on the x -axis. Notice that the curve for the $\lambda = 1.6 \mu\text{m}$ case is the furthest to the left.

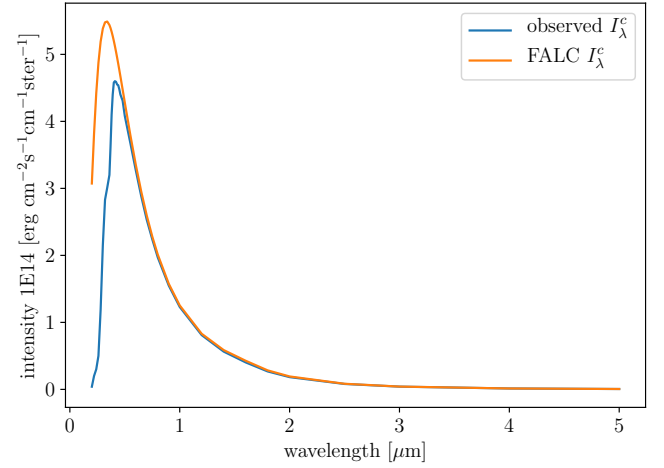


Fig. 9: The emergent intensity as found from Allen (1976) (observed I_λ) and the emergent intensity computed from the FALC model solar temperatures (Fontela et al. 1993) and Allen's wavelengths (FALC I_λ^c). They are shown against the wavelength on the x -axis. They follow each other closely up to the peak at $\lambda \sim 0.5 \mu\text{m}$ where they have a different maximum intensity, the computed FALC intensity having a higher value than Allen's observed intensity.

The emergent intensity computed from the FALC data temperature T for different angles μ against wavelength, can be seen in Figure 10. We see that they all peak for $\lambda = 0.5 \mu\text{m}$, and that the intensity is the largest when the angle $\mu = 1$, meaning when the radiation emerges directly along our sight line.

In Figure 11 we see the emergent solar intensity for wavelengths in the range $\lambda = [0.1, 5] \mu\text{m}$ against the emerging angle of the radiation μ in the range $[0.1, 1]$ in the top frame, and against the apparent solar disk radius $r/R_\odot = \sin \theta$ in the lower frame. We see that the intensity increases with λ , and decreases as we move farther out on the solar limb.

The astrophysical flux computed from the FALC data, along with what was observed by Allen (1976), can be seen in Figure 12. As in Figure 8, the curves are a good fit with each

Table 1: Various values corresponding to the wavelengths in the first column to the left in units of micron. Second, third, and fourth column is the computed emergent intensity (I_λ^{comp}), the observed emergent intensity (I_λ^{obs}), and the best fitted black body curve (B_λ), respectively, all three in units of $\text{erg cm}^{-2} \text{s}^{-1} \text{ster}^{-1} \text{cm}^{-1}$. The two next columns are the ratios between the computed intensity and the emergent intensity, and the computed intensity and the black body intensity. Next is the height at optical thickness $\tau_\lambda = 1$ in km, then follows the mean formation height also in km. Then is the heights corresponding to where the temperature T of the Sun is equal to the brightness temperature T_b (in the last column to the right) in km, notice there are two heights per wavelength. The second to last column is the temperature corresponding to optical depth $\tau_\lambda = 1$.

λ [μm]	I_λ^{comp} [$\text{erg cm}^{-2} \text{s}^{-1} \text{ster}^{-1} \text{cm}^{-1}$]	I_λ^{obs} [$\text{erg cm}^{-2} \text{s}^{-1} \text{ster}^{-1} \text{cm}^{-1}$]	B_λ [$\text{erg cm}^{-2} \text{s}^{-1} \text{ster}^{-1} \text{cm}^{-1}$]	$I_\lambda^{\text{comp}}/I_\lambda^{\text{obs}}$	$I_\lambda^{\text{comp}}/B_\lambda$	$h(\tau_\lambda = 1)$ [km]	$\langle h \rangle$ [km]	$h(T_b = T)$ [km]	$T(\tau_\lambda = 1)$ [K]	T_b [K]
0.5	$4.28 \cdot 10^{14}$	$4.08 \cdot 10^{14}$	$4.66 \cdot 10^{14}$	0.953	0.918	0	-3.17	10.0, 1278.0	6520	6397
1.0	$1.25 \cdot 10^{14}$	$1.23 \cdot 10^{14}$	$1.37 \cdot 10^{14}$	0.982	0.913	10	24.08	20.0, 1065.0	6340	6120
1.6	$4.27 \cdot 10^{13}$	$4.03 \cdot 10^{13}$	$4.65 \cdot 10^{13}$	0.943	0.919	-30	-17.96	-20.0, 1580.0	7280	6938
5.0	$5.74 \cdot 10^{11}$	$5.70 \cdot 10^{11}$	$5.92 \cdot 10^{11}$	0.993	0.970	50	75.90	75.0, 855.0	5790	5654

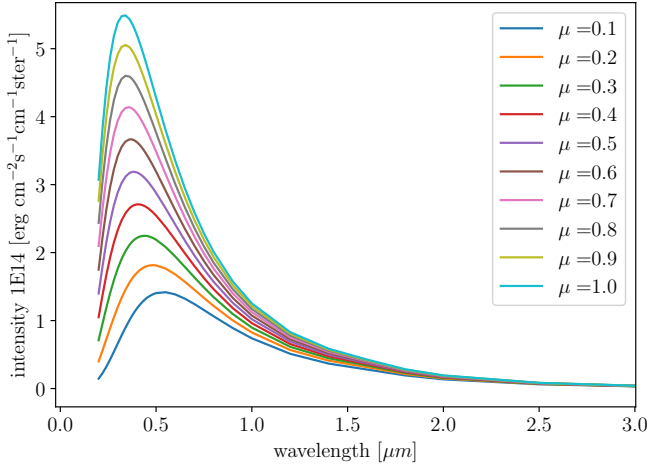


Fig. 10: The computed emergent intensity for different emergence angles $\mu = \cos \theta$ of the radiation against the wavelength λ .

other up their peaks, where they diverge and have different values.

4. Discussion

In Figure 1 we show the emergent intensity and the astrophysical flux of the solar continuum, with and without smoothed lines, as observed by Allen (1976). In Figure 2 we look closer on the intensity without smoothed lines, and compare it to the Planck curve that best fit the intensity. What we see is that for $\lambda > 2 \mu\text{m}$, the curves seem to fit well, but that they start to diverge from one another at $\lambda \sim 1.2 \mu\text{m}$. I_λ^c have a higher maximum intensity than the Planck curve. The reason that the curves has such a noticeable divergence can be that a black body assumes thermodynamic equilibrium and a constant temperature. However, from Figure 3, we see that the brightness temperature is not constant for this body, it is a function of wavelength.

That T_b is not constant, could indicate that we do not have local thermodynamic equilibrium everywhere in the star. The brightness temperature seem to peak at $\lambda = 1.6 \mu\text{m}$, meaning that for this wavelength the Sun is fairly transparent, and that the radiation at this wavelength can escape easier compared to others. This is in the infrared region of wavelengths, meaning that most of the transported radiation is in the infrared. There is also a

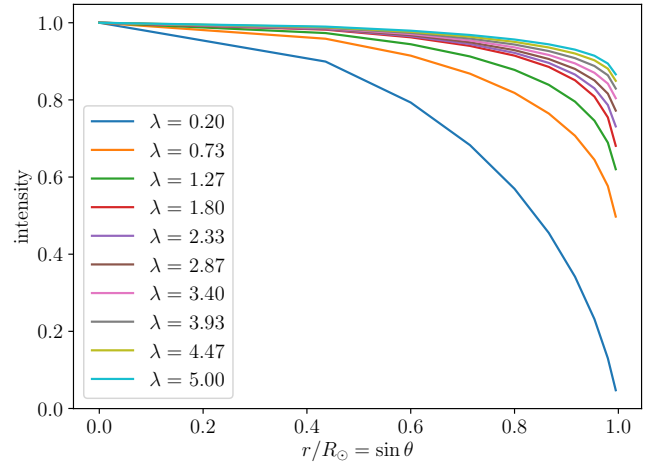
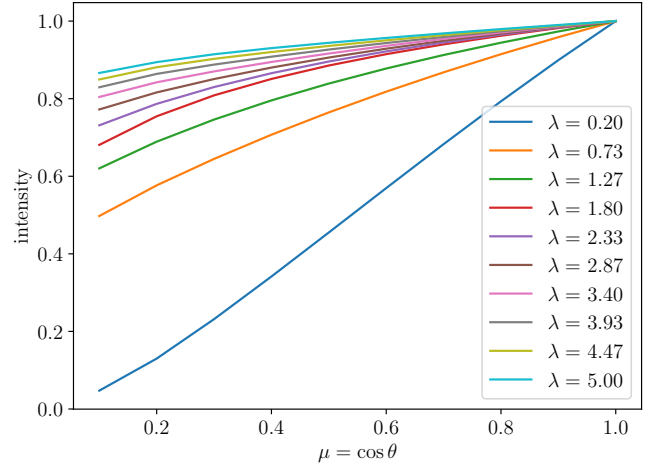


Fig. 11: The normalized emergent intensity for different wavelengths against the angle of the emergent intensity $\mu = \cos \theta$ (top frame), and the apparent solar disk radius $r/R_\odot = \sin \theta$ (lower frame). We see that the intensity increases as the wavelength λ does. It also shows that the intensity decreases toward the edges of the solar disk, but increases with μ .

smaller peak at $\lambda = 0.4 \mu\text{m}$, meaning that a considerable amount of the radiation escape in the UV region as well.

When it comes to the H^- extinction shown in Figure 4 and 5, we see that the shape of the curve is close to the same as the one found by Gray (1992), excluding the H ionization edges.

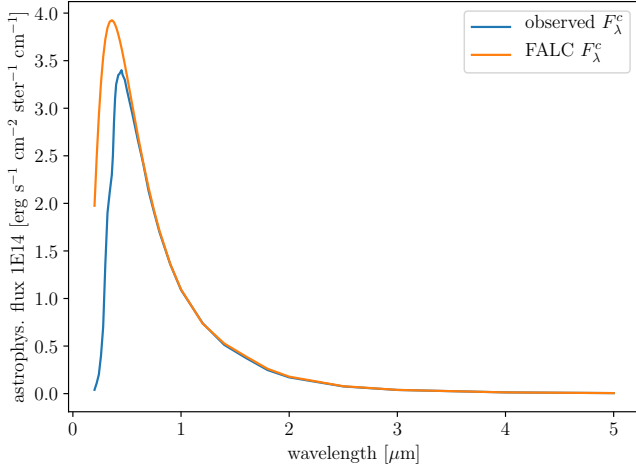


Fig. 12: The computed emergent astrophysical flux (FALC F_{λ}^c) of the solar continuum, and the observed astrophysical flux (Allen 1976) of the Sun (observed F_{λ}^c). As with the intensity in Figure 9, we see that the curves follow each other closely up to their peak, at $\lambda \sim 0.5 \mu\text{m}$, where the computed flux have the highest intensity.

Note that the H^- extinction is not hydrogenic, as the ion has two electrons in its outer shell. This goes to show that H^- is the largest source of extinction in the visible and low infrared wavelength region. We see also that the inversed H^- extinction curve has somewhat the same shape as that of the brightness temperature, which can be seen in Figure 5 where they are overplotted. The peaks in the temperature corresponds to the dips in the extinction, while when the temperature decreases, the extinction increases. This is expected behavior, when the thermal energy in the Sun increases, it gets harder for the hydrogen atom to keep its electrons, due to more frequent collisions and high energetic photons which can ionize the system.

We look next at the total extinction curve α_{λ}^c against height. What we see is that at low altitudes H^- extinction dominates, while after $h = 1000 \text{ km}$, the majority of the extinction comes from Thomson scattering off free electrons. This follows from how at low altitudes we have both a high number density of neutral hydrogen and electrons, making H_{ff}^- extinction possible. Some H_{bf}^- transitions occur also. The Thomson scattering increases for low heights because of the high number density of free electrons, due to the high temperature easily ionizing the elements here, in particular electrons from metals, as seen in the report for Part 1 of this exercise.

The optical depth at $\lambda = 0.5 \mu\text{m}$ in Figure 6 show that the τ_{500} that we compute using the FALC parameters, is a very good fit with the observed optical depth, but as stated, there is a slight deviation. This can come from the fact that we have too few data points to do a proper integration. It could also be that as not all the types of extinction is included in the observed curve, only the bound-free and free-free H^- interactions, it could limit the accuracy of the observed curve, which shows particularly at this height, $h \sim 800 \text{ km}$.

Next we look at the emergent intensity and the height of formation. In Figure 8 it appears that light with a big wavelength form higher up in the atmosphere of the Sun, the exception being for $\lambda = 1.6 \mu\text{m}$, which seem to form at the lowest height compared to the other three wavelengths. This location corresponds to the peak in the brightness temperature, which

also indicated that the intensity here is formed deeper into the star, where the temperature is higher. However, the wavelengths $\lambda = 0.5, 1, 1.6 \mu\text{m}$ all form at around the same height, $h \sim 0 \text{ km}$ to -10 km , while the biggest wavelength $\lambda = 5 \mu\text{m}$ has the largest contribution to emergent radiation at $h \sim 90 \text{ km}$, much higher than the three others. So in general it can seem like the majority of the contribution to the emergent intensity at short wavelengths, occur at low altitudes in the Sun.

From Table 1 we can see that the computed emergent intensity to the observed intensity ratio for the mentioned wavelengths, are at the most 0.993, and 0.943 at the least. The computed intensity compared to the black body intensity B_{λ} have ratios between 0.912 and 0.970. Both of these ratios show that the computed intensity is a good fit with the observed data, and also that the spectrum from a black body is very close to that of the Sun. We see here also that the radiation with a wavelength of $\lambda = 1.6 \mu\text{m}$, have a low mean formation height $\langle h \rangle$, indicating that at this wavelength, the Sun is fairly transparent, the optical depth being one, $\tau_{1600} = 1$, at $h = -30 \text{ km}$. So much of the radiation at this wavelength will escape.

We also wish to know the validity of the Eddington-Barbier approximation $I_{\lambda} \approx B_{\lambda}(T[\tau_{\lambda} = 1])$. We do this by comparing $\langle h \rangle$ with $h(\tau_{\lambda} = 1)$ and $h(T_b = T)$. While $h(\tau_{\lambda} = 1)$ and $\langle h \rangle$ are very close to one another, there is one exception; when $\lambda = 0.5 \mu\text{m}$, where the difference in values is 13.17. If we compare $\langle h \rangle$ to $h(\tau_{\lambda} = 1)$, we see that the values fit the best when $\lambda = 0.5 \mu\text{m}$ the difference being 3 km. For all the other wavelengths, however, the difference between the values are of the order of $\pm 10 \text{ km}$. While ideally these heights should have the same value for the same wavelengths, this is not realistic, as the FALC model assumes a static Sun in hydrostatic equilibrium. Neither have we included the metal bound-free edges, which would affect the extinction and intensity. Still, we consider the discrepancy in height to be within acceptable parameters. Another good analysis tool, is to compare the computed intensity with the Planck curve. If we calculate the ratio $I_{\lambda}/B_{\lambda}(T[\tau_{\lambda} = 1])$, we find that is on average equal to 0.93. We interpret from this that the Planck curve is a very good fit with to the computed intensity. From this we conclude that LTE Eddington-Barbier approximation is valid.

In Figure 9, the solar disk-center intensity spectrum has been computed and plotted together with the observed continuum intensity. As stated, the curves fit each other well with the exception that they have a different maximum intensity. The reason can be that the FALC model assumes LTE, which we have discussed, might not be true throughout the entire Sun, and thereby, not valid at all wavelengths. We see the same for the observed and computed astrophysical flux in Figure 12.

When we take into account that the radiation can emerge at an angle relative to our line of sight, we get Figure 10. As expected, the radiation emerging straight towards us ($\mu = 1, \theta = 0$), has the largest observed intensity. It also shows that at big wavelengths, the angle does not matter, the emergent radiation has the same intensity regardless.

We do the opposite in Figure 11; we plot the intensity against μ and r/R_{\odot} for a select few wavelengths. We see that the intensity decreases near the edges of the solar disk, on the solar limb. The reason the intensity pointing our way is decreasing on the solar limb, is because the height at which $\tau_{\lambda} = 1$ is different here, it lies closer to the surface, at a larger radius. Another effect is that the temperature is often greater the further into the star we go, so at the center it is higher than at the limb, meaning more radiation is produced in the center than at the limb. In Table 1

we show that the height at which $\tau_\lambda = 1$ varies with the wavelength as well, which is why we observe different intensities for different wavelengths. The optical depth varies with wavelength because the optical depth depends on extinction, which is dependent on wavelength.

5. Conclusions

We have looked at the continuous spectrum from the solar atmosphere, concentrating on the visible and near-infrared region of wavelengths. What we found is that the assumption of thermodynamic equilibrium might not be entirely valid everywhere in the star. This is shown by how the brightness temperature T_b is not constant over all wavelengths, and correspondingly, how a Planck curve does not fit with the observed intensity, most notably having a lower maximum intensity and astrophysical flux value. We see this also when comparing the observed intensity, and astrophysical flux from Allen (1976) with ones computed from the FALC model data (Fontela et al. 1993) which assumes LTE: The computed parameters have a larger maximum value than the observed ones, but the curves fit almost perfectly up to the peak, the FALC model is thus a better fit than a black body. The reason for the divergence of the curves in the LTE case, is most likely due to us not including extinction done by metals in our model.

We also found that the radiation with a wavelength of $\lambda = 1.6\mu\text{m}$, have a low mean formation height $\langle h \rangle$, and that at this wavelength, the Sun is fairly transparent, the optical depth being one, $\tau_{1600} = 1$, at $h = -30$ km. So much of this radiation will escape.

We plotted the intensity against $\mu = \cos \theta$ and $r/R_\odot = \sin \theta$, where θ is the emergent angle relative to our line of sight of the radiation, for a select few wavelengths. We see that the intensity decreases near the edges of the solar disk, on the solar limb. We found that this was due to the height at which radiation escapes, $h(\tau_\lambda = 1)$, lies closer to the surface the further to the edges of the solar disk we look. We have shown that the height at which $\tau_\lambda = 1$ varies with the wavelength as well, which is why we observe different intensities for different wavelengths. This is due to the optical depth's dependence on extinction, which is dependent on wavelength.

We found that H^- free-free and bound-free transitions are the major source of extinction in the Sun, along with Thomson scattering off free electrons. This is due to the high number density of both neutral hydrogen and free electrons in the photosphere of the Sun, where the free electrons mostly come from metals with a low ionization energy. Also shown, is that the H^- extinction is very sensitive to temperature, a decrease in T_b agreeing with an increase in H^- extinction.

Comparing the mean formation height $\langle h \rangle$ with $h(\tau_\lambda = 1)$ and $h(T_b = T)$ for different wavelengths, there was a discrepancy in values. While $h(\tau_\lambda = 1)$ and $\langle h \rangle$ are very close to one another, with the exception of when $\lambda = 0.5\mu\text{m}$ where the difference in values is 13.17, when comparing $\langle h \rangle$ to $h(\tau_\lambda = 1)$, we saw that the values fit the best for $\lambda = 0.5\mu\text{m}$ the difference being 3 km. For all the other wavelengths, the difference between the values are of the order 10 km. When comparing the computed intensity with the one obtained from the Planck curve, however, we found that the mean ratio was 0.93, which we consider a very good fit.

Our conclusions are that it is primarily H^- extinction that gives rise to the solar continuum, and that the LTE Eddington-Barbier approximation is a good and valid approximation.

Acknowledgements. We are much indebted to Rob Rutten for exemplary instruction.

6. Appendix

References

- Abramowitz, M. & Stegun, I. 1964, Handbook of mathematical functions with formulas, graphs, and mathematical tables (U.S. Department of Commerce, National Bureau of Standards)
- Allen, C. W. 1976, Astrophysical quantities (London: University of London, Athlone Press)
- Chandrasekhar, S. & Breen, F. 1946, *Astrophys. J.*, 104, 430
- Fontela, J., Avrett, E., & Loeser, R. 1993, *Astrophys. J.*, 409, 319
- Gray, D. F. 1992, *The Observation and Analysis of Stellar Photospheres* (UK: Cambridge University Press)

Analysis of the formation of solar spectral lines with LTE

part 3

Elisabeth Strøm

November 27, 2017

1 Introduction

Here are the results for the third part of the SSB project, where we look at the formation of the Na I D1 spectral line at $\lambda = 5890$ Å. We pull the data from the file `int_nad.dat`, which contains the wavenumbers and the observed spectrum of the Sun.

From the FALC model Fontela et al. (1993) we will use the data of the temperature, hydrogen-,proton- and electron density, the gas pressure, and the microturbulent velocity.

All units are in cgs, unless it is stated otherwise.

2 Results

In Figure 1 we see the solar spectrum over a short wavelength range in both air and vacuum wavelengths. The conversion from the wavenumbers σ to vacuum wavelengths, is given by

$$\lambda_{\text{vac}} = 1/\sigma. \quad (1)$$

The conversion from vacuum wavelengths to air wavelengths, is given by

$$\lambda_{\text{air}} = 0.99972683\lambda_{\text{vac}} + 0.0107 - 196.25/\lambda_{\text{vac}}. \quad (2)$$

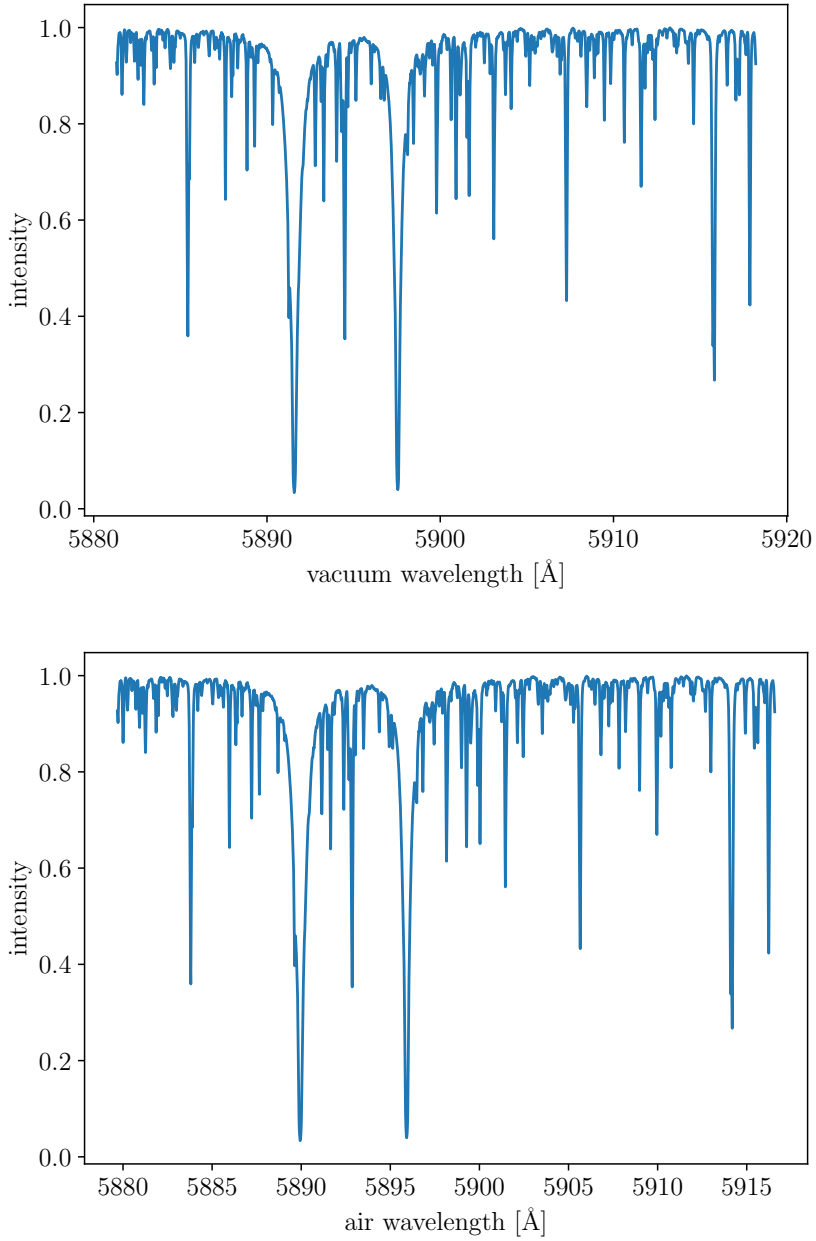


Figure 1: The normalized solar intensity spectrum. The top frame shows the spectrum against vacuum wavelengths, while the lower frame shows the spectrum against the corresponding wavelengths in air. We see the two Na I D lines as the two most pronounced dips in the curve. We find that the vacuum wavelengths of their minimia, are : $\lambda_{\text{vac}}^{\text{Na I D1}} = 5891.58 \text{ \AA}$ and $\lambda_{\text{vac}}^{\text{Na I D2}} = 5897.55 \text{ \AA}$. In air, the wavelengths of the Na I D lines are: $\lambda_{\text{air}}^{\text{Na I D1}} = 5889.95 \text{ \AA}$ and $\lambda_{\text{air}}^{\text{Na I D2}} = 5895.92 \text{ \AA}$. We see that these are in very close agreement with the tabulated solar spectral lines values in Moore et al. (1966).

Next we check that our Boltzmann distribution function and Saha distribution function works. The results can be seen in Figure 2 for the Boltzmann function,

$$\frac{n_{r,s}}{N_r} = \frac{g_{r,s}}{U_r} e^{-\chi_{r,s}/kT} \quad (3)$$

and in Figure 3 for the Saha function,

$$\frac{N_{r+1}}{N_r} = \frac{1}{N_e} \frac{2U_{r+1}}{U_r} \left(\frac{2\pi m_e kT}{h^2} \right)^{3/2} e^{-\chi_r/kT}. \quad (4)$$

Here $g_{r,s}$ is the statistical weights, $\chi_{r,s}$ is the energy of the system at ionization stage r and excitation level s (known from Gray (1992)), k is the Boltzmann constant, T is the temperature, and $N_r = \sum_s n_{r,s}$. Further we have that m_e is the electron mass, and h is the Planck constant, and N_e is the total number density of free electrons. Here U_r is the partition function given by

$$U_r = \sum_s g_{r,s} e^{-\chi_{r,s}/kT}. \quad (5)$$

For Na I, it can be written as

$$U_{\text{NaI}}(T) \approx c_0 + c_1 \log \theta + c_2 \log^2 \theta + c_3 \log^3 \theta + c_4 \log^4 \theta \quad (6)$$

$$U_{\text{NaII}} = 1, \quad U_{\text{NaIII}} = 6 \quad (7)$$

where the values for the constants c_i are known for $i = 1, 2, 3, 4$ (Gray, 1992). θ is defined as $\theta = 5040/T$.

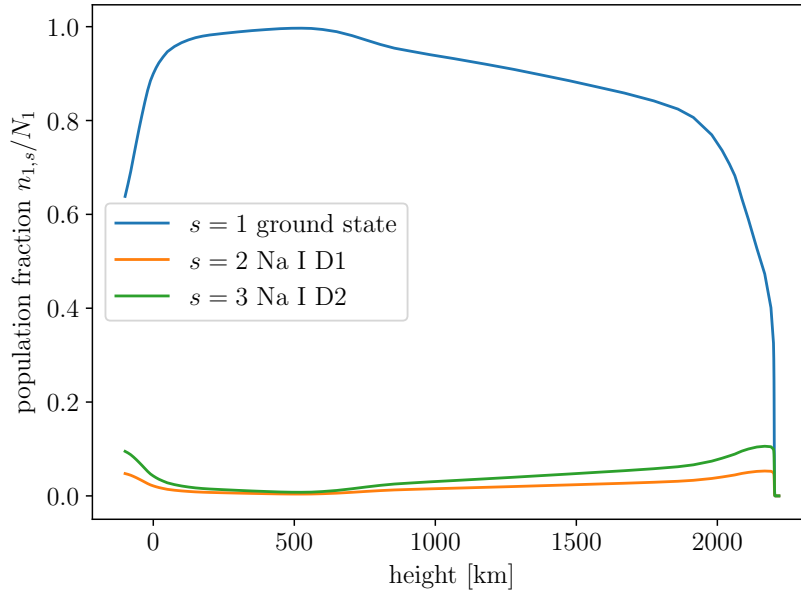


Figure 2: The population fraction for $r = 1$ and $s = 1, 2, 3$. We see that the majority of the sodium I population resides in its ground state, $s = 1$. Less than 20% of the sodium I population are in the first and second excited state. This figure is in concurrence with the one presented in the exercise text.

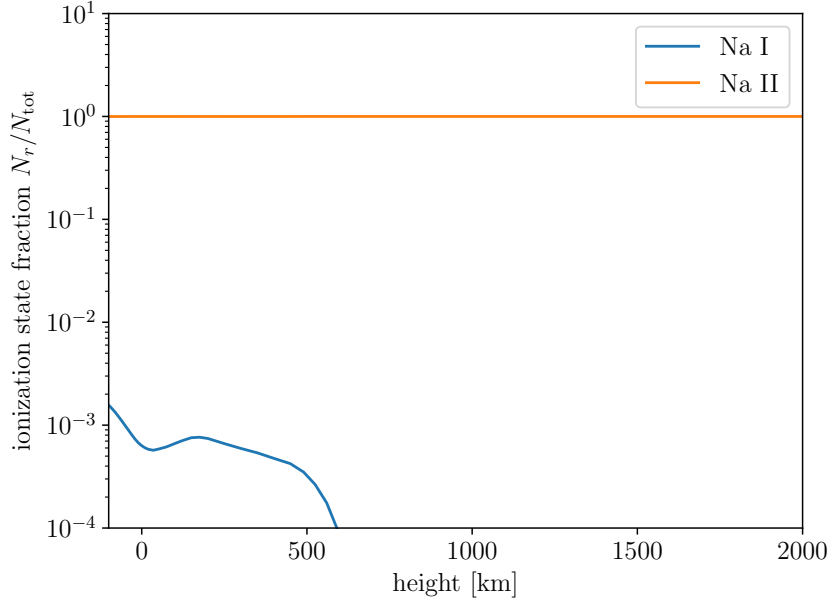


Figure 3: The Saha distribution of sodium for $r = 1$ and $r = 2$. We see that very little sodium is ionized to the first ionization stage, the majority of the population of the element is neutral. Less than 2% of NaI is ionized into NaII, and only on low altitudes. This plot is also in agreement with the one in the exercise text.

The monochromatic line extinction per cm path length for a bound-bound transition between a lower level l and upper level u is given by

$$\alpha_\lambda^l = \frac{\sqrt{\pi}e^2}{m_e c} \frac{\lambda^2}{c} b_l \frac{n_l^{\text{LTE}}}{N_{\text{Na}}} N_H A_E f_{lu} \frac{H(a, v)}{\Delta\lambda_D} \left[1 - \frac{b_u}{b_l} e^{-hc/\lambda kT} \right], \quad (8)$$

where e is the electron charge, and c is the speed of light. $b_l = b_u = 1$ is the population departure coefficients for the lower and upper levels in LTE. The LTE population fraction $n_l^{\text{LTE}}/N_{\text{Na}}$ is given by Saha-Boltzmann distribution, found by multiplying Equation 3 with Equation 4. N_H is here the total number density of neutral hydrogen (Fontela et al., 1993). $A_{\text{Na}} = N_{\text{Na}}/N_H = 1.8 \cdot 10^{-6}$ (Allen, 1976) is the sodium abundance, where N_{Na} is the number density of sodium. The oscillator strength is $f_{lu} = 0.318$ for Na I D1.

We will use `scipy`'s Voigt function, $H(a, v)$, where the parameters a and v is defined as

$$v = \frac{\lambda - \lambda_0}{\Delta\lambda_D} \quad a = \frac{\lambda^2}{4\pi c} \frac{\gamma}{\Delta\lambda_D}. \quad (9)$$

$\gamma = \gamma_{\text{vdW}}$ is the the van der Waals broadening, which depend on T , the gas pressure P_{gas} , the angular quantum number of the level l , and its effective principal quantum number n^* .

The Dopplerwidth is defined as

$$\Delta\lambda_D = \frac{\lambda_0}{c} \sqrt{\frac{2kT}{m_{\text{Na}}} + v_t^2}, \quad (10)$$

where v_t is the micro-turbulent fudge parameter from the FALC model (Fontela et al., 1993), and m_{Na} is the average sodium mass. λ_0 is the wavelength at the center of the spectral lines, for the Na I D1 line, it is $\lambda_{\text{air}}^{\text{Na I D1}}$.

As stated in the second report, we integrate over the extinction to get the optical depth, and thereby the intensity. We add the Na I D1 line found from computing Equation 8, with data from the FALC model (Fontela et al., 1993). The result can be seen in Figure 4.

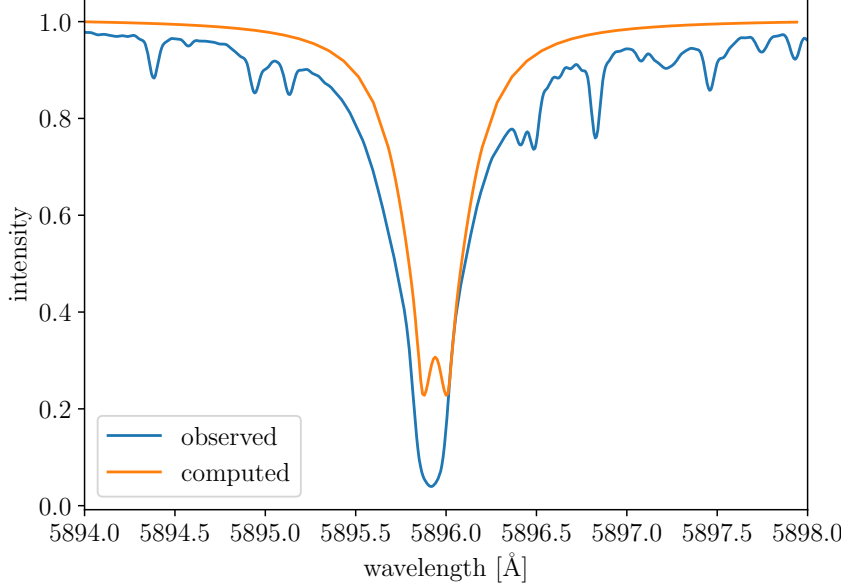


Figure 4: The computed and the observed normalized intensity profile of the Na I D1 line. We see that the computed line has smaller wings and is not broad enough compared to the observed line. The reason for this is that the atomic physics that go into producing the spectral lines, are poorly understood, and so replicating the signal can be difficult. What we could do is include a fudge factor on the van der Waal broadening term. There is also a slight shift in wavelengths between the two lines, the reason for this is unclear. The additional dips in the observed intensity curve comes from extinction from other elements.

The central line core of the computed intensity, also have an intensity reversal in the dip near the minimum value, and is not as dark as in the observed case. The latter is due to our LTE assumption not being valid in the formation of spectral lines. The central-line reversal is due to the temperature we use in our calculation: It has a gradient that changes from negative to positive at some height in our atmosphere.

The minimum intensity is found where T is also minimal. However, the mean height of formation $\langle h \rangle$ (h is height, not the Planck constant here) for the line core, lies at a location that corresponds to where the temperature, and hence the Planck function, has started increasing in the FALC model. That is why it appears that we get emission instead of continued absorption in the central core. On the orange line, what we see as the minimum has a $\langle h \rangle$ that is lower in the atmosphere than line center. And so we get the central-line reversal. A NLTE computation might provide a line profile that better fit the observations.

To make the computed line profile fit better with observations, we add a fudge factor of 2 to the van der Waals broadening term, $\gamma'_{\text{vdW}} = 2\gamma_{\text{vdW}}$. Another way to define the broadening term is $\gamma_{\text{vdW}} = 10^{-7.526}$. This definition comes from the Vienna Atomic line database. Both variations, along with the original computed line, can be seen in Figure 5.

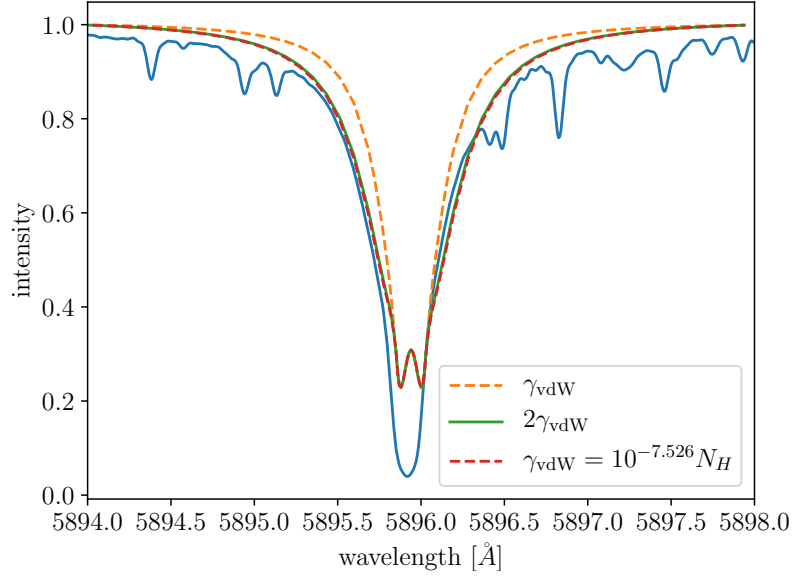


Figure 5: The computed normalized Na I D1 line for three different γ_{vdW} factors. We see that near line center, all the three curves overlap. It is clear that both $\gamma'_{\text{vdW}} = 2\gamma_{\text{vdW}}$ and $\gamma_{\text{vdW}} = 10^{-7.526}$ provide a much better fit to the observed line than the original definition of the van der Waals broadening term did. As for the two new definitions, the curves they produce are hardly separable from one another, $\gamma_{\text{vdW}} = 10^{-7.526}$ giving slightly more broadening.

References

- C. W. Allen. *Astrophysical quantities*. London: University of London, Athlone Press, 1976.
- J.M. Fontela, E.H. Avrett, and R. Loeser. *Astroph. J*, 409:319, 1993.
- D. F. Gray. *The Observation and Analysis of Stellar Photospheres*. UK: Cambridge University Press, September 1992.
- C. E. Moore, M. G. J. Minnaert, and J. Houtgast. *The solar spectrum 2935 Å to 8770 Å*. 1966.